J. Fluid Mech. (1979), *vol.* 93, *part* 1, *pp.* 161–184
Printed in Great Britain

An experimental and numerical study of the secular spin-up of a thermally stratified rotating fluid

By ROBERT C. BEARDSLEY,
Woods Hole Oceanographic Institution, Woods Hole, Mass. 02543

KIM D. SAUNDERS,†
Department of Meteorology, Massachusetts Institute of Technology, Cambridge, Mass. 02139

ALEX C. WARN-VARNAS AND JOHN M. HARDING
Naval Ocean Research and Development Activity, NSTL, Bay St Louis, Miss. 39529

(Received 21 July 1978 and in revised form 31 October 1978)

Laboratory and numerical experiments have been conducted to study the secular spin-up of both a homogeneous and a thermally stratified rotating fluid in a right cylinder. In these experiments, the angular velocity of the container increases linearly in time from some initial rotation rate at $t = 0$. A simple quasi-geostrophic model is developed to describe the adjustment of the fluid over the characteristic spin-up time scale to the constant angular acceleration of the basin. Good agreement is found between the observed interior temperature and azimuthal velocity fields and the theory in both the homogeneous and stratified *secular* experiments. This result is in contrast to the much faster adjustment observed in stratified instantaneous spin-up experiments reported earlier. The main difference between these experimental cases is the inability of secular forcing to excite energetic inertial–gravity-wave transients during the initial phases of secular spin-up. Thus, the asymptotic theory which has filtered out these initial higher-frequency transients is accurate even though the inertial period is not much smaller than the characteristic spin-up time scale.

1. Introduction

Spin-up is the generic name given to the transient motions occurring in a fluid as it adjusts from one state of nearly rigid-body rotation to another. The importance of this spin-up process in rotating homogeneous flows has been clearly explained by Greenspan & Howard (1963) who showed how the viscous Ekman layers could, by means of their suction, induce relatively weak secondary circulations which profoundly affect the interior vorticity and angular momentum fields. By this general mechanism, the Ekman layers completely control the transient spin-up process and bring the interior fluid to its new state of nearly rigid-body rotation in a time scale of $O(H/\sqrt{(\nu\Omega)})$, where Ω is the initial angular velocity of the container and fluid, ν is the kinematic viscosity, and H is a characteristic height of the container. In the case of the spin-up of a

† Present affiliation: NORDA (Code 331), NSTL Building 1100, Bay St Louis, Miss. 39529.

0022-1120/79/4228-6610 $02.00

stratified rotating fluid, Holton (1965) first showed that, even though the Ekman-layer structure is unaffected by stratification, the interior vortex stretching caused by Ekman-layer suction would be balanced by the tilting of the isopycnal surfaces through the thermal-wind relation. Thus in the case of a strongly stratified fluid, the effect of Ekman-layer suction would be limited to horizontal regions (adjacent to the Ekman layers) of vertical scale thickness $\delta = L\Omega/N$, where L is the characteristic horizontal scale of the container and N is the Brunt–Väisälä frequency. The fluid in these layers spins up to the new angular velocity in a time scale of $O(\delta/\sqrt{(\nu\Omega)})$. The remaining interior fluid spins up in the much longer time scales associated with vorticity and density diffusion. The reader is referred to Greenspan (1968) and the review by Benton & Clark (1974) for comprehensive presentations on the general spin-up process, the historical development of relevant conceptual models, and discussions of some of the important geophysical ramifications of the spin-up process.

One of the more interesting applications of spin-up theory in geophysical fluid dynamics arises in the investigation of the internal rotation of the sun. Howard (in an informal seminar in 1970) proposed a hierarchy of rather basic theoretical models to be examined in relation to the solar spin-down mechanism. The first and simplest model is the instantaneous stratified spin-up problem already outlined here and reviewed by Benton & Clark (1974). In the second model, named 'secular' spin-up by Howard, the fluid motion is driven by either the small but constant angular *acceleration* of the fluid container or by a small constant surface *stress*. This latter case is a more realistic model of the sun, where the angular momentum carried away by the solar wind can exert an appreciable torque on the outer layer of the solar atmosphere. Sakurai, Clark & Clark (1971) have examined the stress-driven secular spin-up of a small-Prandtl-number stratified fluid in a cylindrical container while Clark *et al.* (1972) have studied the spherical problem for a stratified fluid of Prandtl number of $O(1)$. The two-dimensional stress-driven stratified spin-up problem has also been examined by Pedlosky (1968), Allen (1973), Blumsack (1972) and others as a fundamental conceptual model of coastal upwelling.

We will present in this paper the results of an experimental and numerical study of the secular spin-up of a rotating thermally stratified Boussinesq fluid. The fluid container is cylindrical in shape and the fluid used has a large Prandtl number. As such, this work represents a logical extension of both the experimental studies of the instantaneous spin-up of a stratified rotating fluid conducted earlier by Buzyna & Veronis (1971) and Saunders & Beardsley (1975), and the corresponding numerical simulations of instantaneous stratified spin-up made by Barcilon *et al.* (1975). In these experiments, the angular velocity of the rotating cylindrical fluid container was rapidly changed by a small fraction and the resulting baroclinic adjustment by which the fluid spins up to the new angular velocity was investigated. The results of these experiments indicated that the interior of the fluid spins up more rapidly than predicted by the quasi-geostrophic spin-up theories developed by Siegmann (1967), Walin (1969) and Sakurai (1969). Barcilon *et al.* (1975) obtained numerical solutions to the full axisymmetric problem and also found faster spin-up in the parameter range studied (see Saunders & Beardsley (1975) for a comparison of the observed experimental temperature field with the numerically predicted field). Barcilon *et al.* (1975) also observed that the corner jet which closes the secondary circulation driven by the Ekman-layer suction is time-dependent over the spin-up time scale: the fluid in the

corner jet appeared to remain nearer the vertical side wall initially and thus gained more angular momentum due to lateral viscous diffusion of vorticity from the side wall during the early phases of spin-up than predicted. In most of these numerical experiments and in the preceding laboratory experiment, the characteristic spin-up time scale was not much greater than the rotation period, a condition which tended to strain the validity of the quasi-geostrophic theory which has filtered out the initial inertial–gravity-wave transients. Benton & Clark (1974) conclude that the flow observed in these experiments was clearly more complicated than that predicted by the quasi-geostrophic theory; however, a proper experimental test of this theory will require experiments in which the spin-up time scales for the dominant modes are much greater than both the rotation and the Brunt–Väisälä periods. To our knowledge, such experiments (either laboratory or numerical) have not been conducted. A second, alternative explanation for the observed discrepancy between experimental and predicted spin-up has been suggested by St-Maurice & Veronis (1975), who re-examined the instantaneous stratified spin-up problem using the method of multiple time scales. In essence, they attempted to find interior and boundary-layer solutions uniformly valid over the *three* important time scales, i.e. the rotation period, the longer spin-up time, and the much longer diffusive time scale which governs the final adjustment of the fluid to the new state of solid-body rotation. Their complete solution for the interior flow during stratified spin-up does contain a diffusive part which can be numerically significant on the spin-up time scale. The model problem which they consider has a simple one-dimensional periodic horizontal dependence and thus does not include the influence of lateral boundaries. Since Barcilon *et al.* (1975) have demonstrated that the structure of the flow near the lateral boundaries is clearly important in the laboratory and numerical experiments conducted in a cylindrical container, the diffusive correction found by St-Maurice & Veronis (1975) may not be applicable to the cylindrical problem. We are unaware of any laboratory or numerical spin-up experiments which have been studied over the diffusive time scale.

In this present study of secular spin-up, the angular velocity of the fluid container is changed linearly with time such that the non-dimensionalized angular acceleration is small. Our interest is focused on the fluid motions occurring on the basic spin-up time scale and to this end we will next present the simple quasi-geostrophic theory for secular stratified spin-up in §2, which we will later compare with the experimental temperature and velocity fields in §4. The laboratory apparatus and experimental procedures and the numerical model are described in §3. An analysis of one homogeneous secular spin-up experiment is also presented in §4.

2. Theoretical model

A linear asymptotic model for instantaneous stratified spin-up in a cylindrical container with perfect insulating side boundaries has been thoroughly discussed by Walin (1969) and Sakurai (1969). We will derive here the modification of this model introduced by a small but constant angular acceleration of the fluid container. The equations considered are the usual Boussinesq approximation to the Navier–Stokes equations. We neglect the centrifugal component of the gravitational potential (thus neglecting Sweet–Eddington flow) and assume that the basic density stratification is linear with depth. This basic density state is maintained by a continuous vertical heat

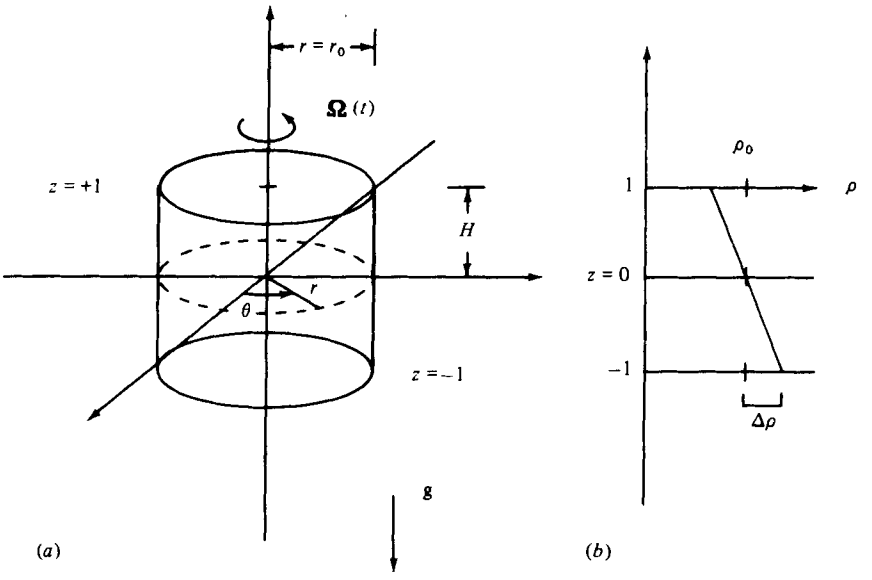

FIGURE 1. (*a*) Model geometry. (*b*) Basic density profile.

flux through the fluid. The temperatures on the upper and lower surfaces are held at $T_0+\Delta T$ and $T_0-\Delta T$ respectively. The equation of state is simply

$$\rho = \rho_0(1-\alpha(T-T_0)),$$

where ρ_0 and T_0 are the mean density and temperature respectively and α is the assumed constant coefficient of thermal expansion. The coefficients of thermal diffusivity κ and kinematic viscosity ν are also assumed constant. The fluid container and forcing, and thus the response, are taken to be axisymmetric. The co-ordinate system used is the r, θ, z cylindrical system. The length scale is chosen as the half-height of the cylinder H so that the cylinder is bounded above and below at non-dimensional heights $z = +1$ and -1 respectively (see figure 1). The non-dimensional radius or aspect ratio of the cylinder is denoted by r_0, and is assumed here to be of order unity.

At $t = 0$, the angular velocity of the container starts to increase linearly from an initial value Ω_0, i.e. $\Omega(t) = \Omega_0 + (d\Omega/dt)t$ for $t \geqslant 0$, where the angular acceleration $d\Omega/dt$ is assumed to be constant. In the reference frame which continues to rotate at the original angular velocity Ω_0 of the container, the interior fluid is forced from an initial state of rest by Ekman suction driven by the relative motion of the container top and bottom surfaces. Independent of the interior response, however, the azimuthal velocity scale V within the Ekman layers during spin-up is

$$V = H\frac{d\Omega}{dt}T_s, \tag{1}$$

where $T_s \equiv 1/\Omega_0 E^{\frac{1}{2}}$ is the characteristic homogeneous spin-up time scale. We will use H, V, and T_s as the appropriate length, velocity, and time scales and introduce the non-dimensional perturbation velocity, temperature, and pressure variables defined by

$$\mathbf{u}_* = V\mathbf{u}, \quad T_* = \frac{\Omega_0 V}{\alpha g}T, \quad p_* = \rho_0\Omega_0 HVp,$$

where an asterisk denotes a dimensional variable. The principal non-dimensional parameters governing secular spin-up are the Rossby number R, Ekman number E, Prandtl number σ, and the stratification parameter B defined here by

$$R = \frac{V}{\Omega_0 H}, \quad E = \frac{\nu}{\Omega_0 H^2}, \quad \sigma = \frac{\nu}{\kappa}, \quad B = \frac{N}{2\Omega_0},$$

where N is the Brunt–Väisälä frequency given by $N^2 \equiv \alpha g \Delta T/H$. We will assume that the angular acceleration rate $d\Omega/dt$ is sufficiently small ($d\Omega/dt \ll \Omega_0/T_s$) that the flow is essentially linear, i.e. $R \ll 1$. We will also assume that $E \ll 1$, and both B and the Prandtl number σ are of order unity. With these assumptions the linearized and scaled continuity, momentum, and energy equations are

$$E^{\frac{1}{2}} u_t - 2v = -p_r + E\mathscr{L}u,$$

$$E^{\frac{1}{2}} v_t + 2u = +E\mathscr{L}v,$$

$$E^{\frac{1}{2}} w_t = -p_z + E\nabla^2 w + T,$$

$$E^{\frac{1}{2}} T_t + 4B^2 w = (E/\sigma)\nabla^2 T,$$

$$\frac{1}{r}(ru)_r + w_z = 0,$$

where the operator $\mathscr{L}$ is defined by

$$\mathscr{L}(f) = \nabla^2 f - \frac{f}{r^2} = \left(\frac{1}{r}(rf)_r\right)_r + f_{zz}.$$

The fluid is initially at rest and the boundary condition in the original reference frame is simply

$$\mathbf{u} = rt\hat{\boldsymbol{\theta}}$$

on all surfaces of the container.

Following the general approach presented by Greenspan (1968), we solve the resulting combined initial-value–boundary-value problem for the interior flow using the method of matched asymptotic expansions. The axisymmetric velocity field is defined by $\mathbf{u} = v\hat{\boldsymbol{\theta}} + \nabla \times (\psi\hat{\boldsymbol{\theta}})$. The streamfunction Ψ in the r, z plane is related to ψ by $r\psi = \Psi$. We expand the dependent variables into interior and boundary-layer components using the perturbation series

$$\psi = \psi_0 + E^{\frac{1}{4}}\psi_1 + E^{\frac{1}{2}}\psi_2 + \ldots + \hat{\psi}_0 + E^{\frac{1}{4}}\hat{\psi}_1 + E^{\frac{1}{2}}\hat{\psi}_2 + \ldots,$$

where the carets denote the boundary-layer correction fields. The choice of velocity scale stated in (1) implies that an $O(1)$ azimuthal flow will develop on the homogeneous spin-up time scale, thus forcing the meridional circulation to be $O(E^{\frac{1}{2}})$ by Ekman suction. The lowest-order interior momentum and temperature equations then reduce to

$$2v_0 = p_{0r}, \quad v_{0t} - 2\psi_{2z} = 0, \quad 0 = -p_{0z} + T_0, \quad T_{0t} + 4B^2\left(\frac{r\psi_2}{r}\right)_r = 0. \tag{2}$$

These interior equations may be combined to show the thermal-wind balance

$$2v_{0z} = T_{0r} \tag{3}$$

and conservation of potential vorticity Γ_0

$$\frac{\partial}{\partial t}\Gamma_0 = \frac{\partial}{\partial t}\left(\frac{1}{r}(rv_0)_r - \frac{1}{2B^2}T_{0z}\right) = 0 \tag{4}$$

over the spin-up time scale. (Since the non-dimensional azimuthal velocity in the reference frame *fixed* to the container, called the accelerating frame or AF, is related to V_0 in the original reference frame by the transformation

$$v_0(\mathrm{AF}) = v_0 - rt, \tag{5}$$

the potential vorticity of a fluid particle as viewed in the accelerating frame must decrease from zero everywhere in the interior at a constant rate, i.e. $\Gamma_{0t}(\mathrm{AF}) = -2$.) Conservation of potential vorticity in the original co-ordinate frame also implies that the interior flow obey the elliptic equation

$$\frac{1}{r}(r\psi_{2r})_r + \frac{1}{B^2}\psi_{2zz} = 0 \tag{6}$$

(which is identical in form in either co-ordinate frame).

The fluid must satisfy the no-slip boundary condition in the accelerating frame so that a boundary-layer analysis of the Ekman layers at $z = \pm 1$ yields for the Ekman suction relation

$$\psi_2 = \mp \tfrac{1}{2}(v_0 - rt) \quad \text{at} \quad z = \pm 1.$$

This may then be combined with the interior azimuthal momentum balance to yield an Ekman-layer compatibility condition on ψ_2 that

$$\psi_{2t} = \mp (\psi_{2z} - \tfrac{1}{2}r) \quad \text{at} \quad z = \pm 1. \tag{7}$$

This expression clearly illustrates that the interior motions are forced by the boundary-layer suction of the quasi-steady Ekman layers which form on the accelerating horizontal surfaces. This compatibility condition and the governing potential-vorticity conservation equation (6) together with the appropriate side-wall boundary condition then uniquely specify the lowest-order meridional flow ψ_2 and indirectly v_0. We will now discuss the side-wall matching condition.

There are two boundary layers present on the side boundary: a transient $O(E^{\frac{1}{4}})$ Stewartson layer, which serves to adjust the tangential velocity discontinuity at the wall, and a quasi-steady $O(E^{\frac{1}{2}})$ buoyancy layer, which serves to adjust the temperature gradient and vertical velocity at the side wall. Saunders & Beardsley (1975) show through an analysis of the buoyancy layer in the geometry relevant to these experiments that the side boundary may be considered (with very little error) to be a perfect thermal insulator. Pedlosky (1968) has shown for the case of a perfectly insulated side wall that the vertical motion in the buoyancy layer is so strongly inhibited by the local buoyancy forces that the vertical boundary layer cannot carry any of the mass flux of the Ekman layers. The Ekman-layer flux is thus forced to return directly to the interior from the corner regions in order to close the secondary meridional circulation. This means that there is no radial influx into the interior from the side wall, the buoyancy layer vanishes to lowest order and the boundary becomes a streamline for the interior flow, so that

$$\psi_2 = 0 \quad \text{at} \quad r = r_0. \tag{8}$$

This vanishing of the interior radial velocity at the side boundary implies through the azimuthal momentum balance (2) that the interior zonal flow v_0 remain equal to 0 at the side boundary, and, by Kelvin's theorem, the horizontal averaged interior vorticity at any level is

$$\langle \zeta_0 \rangle = 2\pi \int_r^{r_0} \zeta_0 \, r \, dr = 0$$

over the spin-up time scale. Ekman suction causes interior vortex stretching and shrinking near the centre and outer boundary respectively, which shifts positive vorticity towards the centre without changing the total vorticity. This redistribution of relative vorticity causes a net increase in the angular momentum $\langle rv_0 \rangle$ within that layer. Note that in the completely inviscid problem (i.e. with no viscous boundary layers developing on any surfaces), the interior fluid locally conserves its angular momentum and continues to move in solid-body rotation with an absolute angular velocity of Ω_0. This latter state is characterized by the relative zonal velocity field $v_0 = -rt$ (for $t > 0$) when viewed in the accelerating reference frame.

In the viscous case studied here, a transient $E^{\frac{1}{4}}$ Stewartson layer develops on the vertical side wall which forces the zonal flow to satisfy the no-slip condition at the side boundary. As pointed out by Barcilon (1968), this time-dependent $E^{\frac{1}{4}}$ layer is essentially a Rayleigh-type viscous diffusive layer which grows to a scale thickness of $O(E^{\frac{1}{4}})$ on the spin-up time scale. (The reader is referred to Barcilon (1968) for a derivation and discussion of the equations governing the time-dependent $E^{\frac{1}{4}}$ Stewartson layer in a homogeneous fluid and to Buzyna & Veronis (1971) for a discussion of and observation of the transient $E^{\frac{1}{4}}$ layer made in their experimental study of instantaneous stratified spin-up.) In this problem, the vertical velocity in the transient $E^{\frac{1}{4}}$ Stewartson layer is sufficiently inhibited by the basic stratification that the zonal component of the boundary-layer correction velocity satisfies the one-dimensional viscous diffusion equation

$$\hat{v}_{0t} = \hat{v}_{0\rho\rho}, \tag{9}$$

where the stretched side-wall co-ordinate is defined by $\rho = E^{\frac{1}{4}}(r - r_0)$. As we will see, the local viscous–diffusion balance stated in (9) must change near the corner regions where relatively strong vertical velocities do occur near the side boundary.

The solutions for the lowest-order interior velocity and temperature fields are then

$$\psi_2 = \Sigma \frac{C_n}{2m_n}(1 - e^{-\beta_n t}) \frac{\sinh m_n z}{\cosh m_n} J_1\left(\frac{\alpha_n r}{r_0}\right), \tag{10}$$

$$v_0 = +\Sigma \frac{C_n}{\beta_n}(\beta_n t + e^{-\beta_n t} - 1) \frac{\cosh m_n z}{\cosh m_n} J_1\left(\frac{\alpha_n r}{r_0}\right) + r_0\{(t + \tfrac{1}{2}\rho^2) \operatorname{erfc}(\rho/2t^{\frac{1}{2}}) - \rho(t/\pi)^{\frac{1}{2}} e^{-\rho^2/4t}\}, \tag{11}$$

$$T_0 = -\Sigma 2B \frac{C_n}{\beta_n}(\beta_n t + e^{-\beta_n t} - 1) \frac{\sinh m_n z}{\cosh m_n} J_0\left(\frac{\alpha_n r}{r_0}\right), \tag{12}$$

where $m_n = B\alpha_n / r_0$, $\beta_n = m_n \cosh m_n$, α_n is the nth root of the J_1 Bessel function, erfc is the complementary error function, and ρ is the stretched co-ordinate defined earlier for the transient $E^{\frac{1}{4}}$ side-wall layer. The coefficients C_n are defined by the Bessel–Fourier expansion

$$r = \Sigma C_n J_1(\alpha_n r / r_0),$$

so that

$$C_n = -2r_0 / \alpha_n J_0(\alpha_n).$$

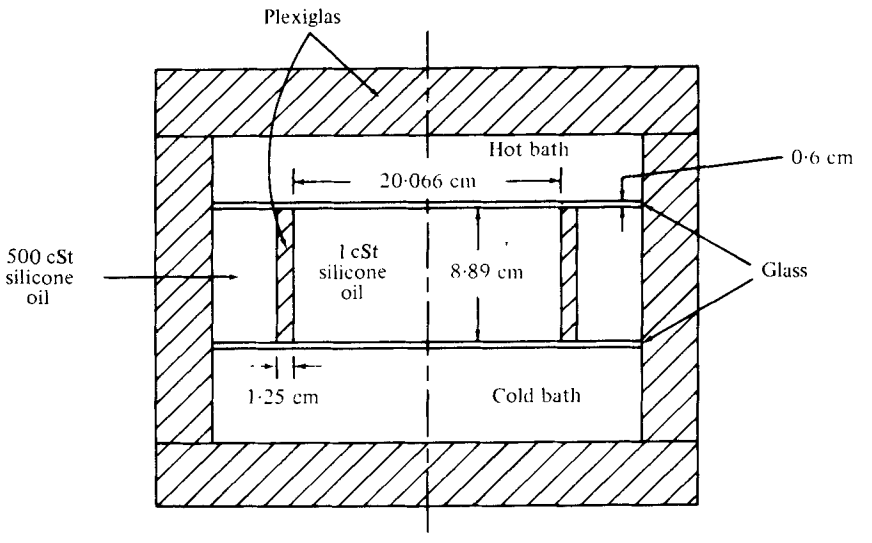

FIGURE 2. Schematic diagram of the test cell.

The interior solutions are composed of an infinite set of modes with each mode decaying with distance away from the end plates at $z = \pm 1$. The characteristic vertical penetration scale of each mode δ_v is related to the characteristic horizontal length scale $\delta_r \equiv r_0/\alpha_n$ by the conservation of potential vorticity constraint (6) which requires that $B\delta_v/\delta_r \sim 1$. As mentioned before, each mode then spins up in its own non-dimensional time scale of $O(\beta_n^{-1})$. This is the same time scale as for a homogeneous fluid of thickness δ_v. Since we will use these solutions to help describe the experimental results, we will postpone our discussion of their properties until after the experimental apparatus and procedure and the numerical models are briefly described.

3. Experimental and numerical work

3.1. *Experimental apparatus and procedure*

The basic experimental apparatus used in these experiments on secular spin-up has been described in detail in the earlier study of instantaneous spin-up by Saunders & Beardsley (1975). A brief summary of that description will be given next for completeness. The fluid container consisted of a Plexiglas cylinder 8·89 cm high and 10·03 cm in radius (see figure 2). The wall thickness of the cylinder was about 1 cm. This cylinder was bounded on the top and bottom by 0·6 cm thick glass plates, glass being chosen for its relatively high thermal conductivity and optical transparency. The cylinder and glass plates were sealed inside a larger Plexiglas box with spaces arranged above and below the glass plates for the circulation of heating and cooling water. The interior of the cylinder was filled with 0·01 cm^2/s (nominal) viscosity silicone oil. This oil was chosen as the working fluid for its relatively large coefficient of thermal expansion and low electrical conductivity; this latter property allowed the use of uninsulated thermistors in monitoring the internal temperature of the fluid. As shown in figure 2, the space surrounding the cylinder between the glass plates was filled with a high viscosity silicone oil; the rapid spin-up of this surrounding fluid was intended to decrease the

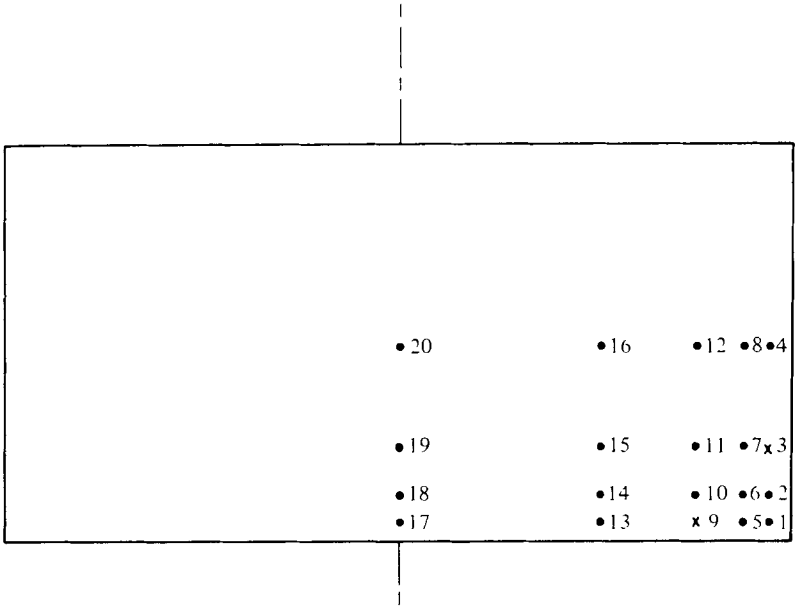

FIGURE 3. Thermistor positions and numbering scheme. The co-ordinates (r, z) of thermistor number n are listed as $n(r/r_0, z)$: 1(0·9375, −0·875) 2(0·9375, −0·750); 3(0·9375, −0·500); 4(0·9375, 0); 5(0·875, −0·875); 6(0·875, −0·750); 7(0·875, −0·500); 8(0·875, 0); 9(0·750, −0·875); 10(0·750, −0·750); 11(0·750, −0·500); 12(0·750, 0); 13(0·500, −0·875); 14(0·500, −0·750); 15(0·500, −0·500); 16(0·500, 0); 17(0, −0·875); 18(0, −0·750); 19(0, −0·500); 20(0, 0). Thermistors 3 and 9 are broken.

radial heat flux and improve the perfectly insulating side wall approximation made in § 2.

The box containing the fluid test section was mounted on an ultra-stable air-bearing turntable designed for these spin-up experiments by Saunders & Beardsley (1975). The turntable was directly driven by a small synchronous motor and, for the experiments described, a typical rotation rate $\Omega_0 = 1$ rad/s was used. A constant angular acceleration of the turntable was obtained in the following manner. The output of a voltage-controlled oscillator driven by a linear-ramp generator was amplified and fed to the synchronous motor driving the table. The angular velocity of the table was then a linearly increasing function of time and the adjustable slope of the ramp function set the rate of angular acceleration.

The vertical temperature gradient in the test section was maintained by heating the upper plate and cooling the lower plate by running hot and cold water through the spaces above and below the glass plates respectively. The temperature was controlled by two larger constant-temperature water baths to within ± 0·05 °C. The temperature on the upper side of the bottom plate was found to vary by less than ± 0·02 °C during a typical experiment. A typical temperature difference of 8 °C was maintained between the two water baths.

The fluid temperature field was measured using 18 thermistors placed in the interior of the test cylinder. Twenty thermistors were originally available, but two had failed and could not be easily replaced for these sets of experiments. The location of the thermistors is shown in figure 3. The nominal diameter of a thermistor was 0·025 cm and

0·005 cm diameter wire was used to suspend the thermistors along radii of the cylinder. The estimated torque exerted on the fluid by the drag of the wires and thermistors is insignificant in comparison with the torque exerted by the solid boundaries.

The fluid temperature data were taken sequentially by means of a computer-controlled stepping switch which changed the thermistor in the appropriate arm of a Wheatstone bridge. The order of sampling was the same as the numbering scheme of the thermistors. The time needed to sample all the thermistors was about 4·5 s or typically somewhat less than one rotation period. The analog output of the Wheatstone bridge was then amplified, low-pass filtered, and digitized using an analog to digital (A/D) converter controlled by a minicomputer. Before beginning a run, the system was allowed to spin up for 2–4 h. When the interior had reached thermal equilibrium as determined from the thermistor output, the experiment was started, i.e. both the angular acceleration or deacceleration of the apparatus and the temperature sampling program began. Data was then usually acquired for the next four or five homogeneous spin-up times.

3.2. *The numerical model*

The numerical scheme used here to simulate the laboratory spin-up experiments employed finite-difference formulations of the full axisymmetric Boussinesq Navier–Stokes equations written in cylindrical co-ordinates, i.e.

$$\frac{\partial u}{\partial t} = -\frac{1}{r}\frac{\partial}{\partial r}(ruu) - \frac{\partial}{\partial z}(uw) + \left(2\Omega + \frac{v}{r}\right)v - \frac{1}{\rho_0}\frac{\partial p}{\partial r} + \nu\left[\frac{\partial}{\partial r}\frac{1}{r}\frac{\partial}{\partial r}(ru) + \frac{\partial^2 u}{\partial z^2}\right], \tag{13}$$

$$\frac{\partial v}{\partial t} = -\frac{1}{r}\frac{\partial}{\partial r}(ruv) - \frac{\partial}{\partial z}(vw) - \left(2\Omega + \frac{v}{r}\right)u + \nu\left[\frac{\partial}{\partial r}\frac{1}{r}\frac{\partial}{\partial r}(rv) + \frac{\partial^2 v}{\partial z^2}\right], \tag{14}$$

$$\frac{\partial w}{\partial t} = -\frac{1}{r}\frac{\partial}{\partial r}(ruw) - \frac{\partial}{\partial z}(ww) - \frac{1}{\rho_0}\frac{\partial p}{\partial z} + \nu\left[\frac{1}{r}\frac{\partial}{\partial r}\left(r\frac{\partial w}{\partial r}\right) + \frac{\partial^2 w}{\partial z^2}\right] + \alpha g T, \tag{15}$$

where p denotes the pressure and ρ_0 the reference density. The equations for temperature and continuity are

$$\frac{\partial T}{\partial t} = -\frac{1}{r}\frac{\partial}{\partial r}(ruT) - \frac{\partial}{\partial z}(wT) + K\left[\frac{1}{r}\frac{\partial}{\partial r}\left(r\frac{\partial T}{\partial r}\right) + \frac{\partial^2 T}{\partial z^2}\right]g, \tag{16}$$

$$\frac{1}{r}\frac{\partial}{\partial r}(ru) + \frac{\partial w}{\partial z} = 0. \tag{17}$$

We shall first discuss the stretching of the grid mesh and the spatial differencing, then the time differencing and the method used to find the pressure. The stretching of the mesh was accomplished by the use of the function $\xi = (e^{r/r_l} - 1)/(e^{r/r_l} + 1)$, where r_l is a normalization constant that controls the stretching in the lth boundary layer. For equal increments $\Delta\xi$ of the function $\xi_i = i\Delta\xi$, a set of co-ordinate values r_i can be generated such that $\Delta r = r_i - r_{i-1}$ constitute the variable mesh spacings. A similar transformation is effected between η and z. It must be pointed out that the equations are not transformed to a new co-ordinate system ξ and η, but are directly differenced on the new grids r_i and z_k; the functions ξ and η merely serve the purpose of creating a smoothly varying r and z mesh. The grid was stretched in order to resolve the relevant

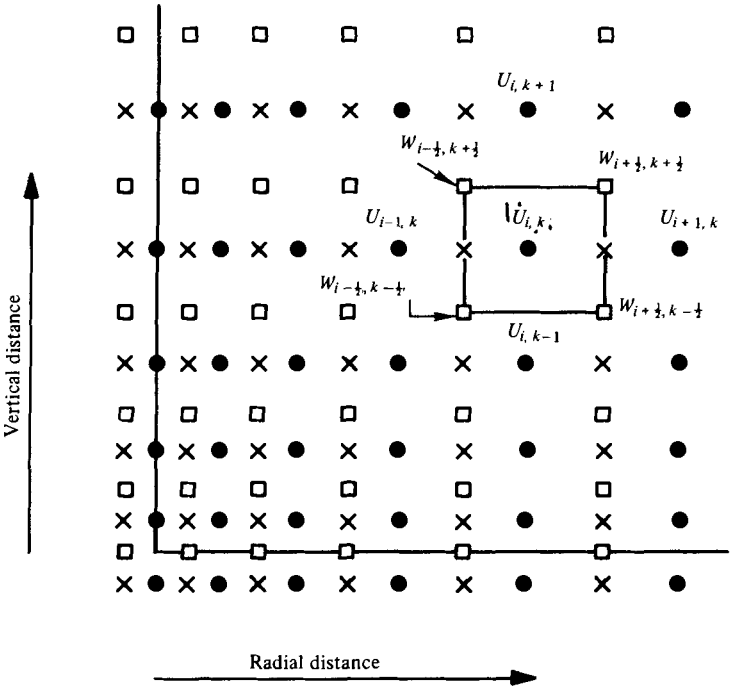

FIGURE 4. Numerical grid schematic, showing the locations of different grid nets used to compute the different dependent variables. □, vertical velocity; ●, radial velocity; ×, zonal velocity pressure.

boundary layers. The criteria used to resolve the Ekman layer are described in Warn-Varnas *et al.* (1978).

The differencing of the advection terms will be illustrated on the transport part of the radial velocity equation (13). The scheme was presented for constant grids by Piacsek & Williams (1970). We shall denote the co-ordinate axes by r_i and z_k, the time by $t_n = n\Delta t$, and the value of a dependent variable ϕ as $\phi(r_i, z_k, t_n) = \phi^n_{i,k}$ with the superscript denoting a time level and the subscripts a mesh point location in space. Reference should be made to figure 4 for inspecting the arrangement of the dependent variables on the various subsets of the staggered mesh. Using these symbols, we have

$$\frac{1}{4r_i\,\Delta r_{i+\frac{1}{2}}}[r_{i+\frac{1}{2}}(u_{i+1}+u_i)\,u_{i+1}-r_{i-\frac{1}{2}}(u_i+u_{i-1})\,u_{i-1}]_k$$
$$+\frac{1}{4\Delta z_{k+\frac{1}{2}}}[(w_{i+\frac{1}{2}}+w_{i-\frac{1}{2}})_{k+\frac{1}{2}}\,u_{i,k+1}-(w_{i+\frac{1}{2}}+w_{i-\frac{1}{2}})_{k-\frac{1}{2}}\,u_{i,k-1}].$$

The remaining terms in (13) are differenced as follows:

(*a*) the pressure term,

$$-\frac{1}{\rho}\frac{1}{\Delta r_{i+\frac{1}{2}}}(p_{i+\frac{1}{2}}-p_{i-\frac{1}{2}})_k;$$

(*b*) the Coriolis and curvature term,

$$\left[2\Omega_f+\frac{1}{2}\left(\frac{v_{i+\frac{1}{2}}}{r_{i+\frac{1}{2}}}+\frac{v_{i-\frac{1}{2}}}{r_{i-\frac{1}{2}}}\right)_k\right]\times\tfrac{1}{2}(v_{i+\frac{1}{2}}+v_{i-\frac{1}{2}})_k;$$

and (*c*) the friction terms,

$$\nu\left\{\frac{1}{\Delta r_{i+\frac{1}{2}}}\left[\frac{1}{r_{i+\frac{1}{2}}}\frac{1}{\Delta r_{i+1}}(r_{i+1}u_{i+1}-r_i u_i)-\frac{1}{r_{i-\frac{1}{2}}}\frac{1}{\Delta r_i}(r_i u_i-r_{i-1}u_{i-1})_k\right]\right.$$
$$\left.+\frac{1}{\Delta z_{k+\frac{1}{2}}}\left[\frac{1}{\Delta z_{k+1}}(u_{k+1}-u_k)_i-\frac{1}{\Delta z_k}(u_k-u_{k-1})_i\right]\right\}.$$

The pressure is found from a Poisson's equation obtained from taking the divergence of the system (13) and (15). Thus

$$\frac{\partial D}{\partial t}=-\nabla^2 p+\nabla.\{\mathbf{A}+\mathbf{C}+\mathbf{F}+\mathbf{E}\}, \tag{18}$$

where $\mathbf{A}(A_u, A_w)$, $\mathbf{C}(C_u, 0)$, $\mathbf{F}(F_u, F_w)$, and $\mathbf{E}(0, \alpha g T)$ are the advection, Coriolis, friction, and external force terms in the u and w equations, respectively. The time differencing of the system can be represented using the same notation as

$$\frac{u_l^{n+1}-u_l^{n-1}}{2\Delta t}=p_l^n+A_l^n+C_l^n+F_l^{n+1,n,n-1}+E_l^n,$$

where $l = u, v, w$ and $F_l^{n+1,n,n-1}$ is the Dufort–Frankel scheme given by

$$\frac{1}{\Delta x_{i+\frac{1}{2}}}\left[\frac{(\phi_{i+1}^n-\phi_i^{n+1})}{\Delta x_{i+1}}-\frac{(\phi_i^{n-1}-\phi_{i-1}^n)}{\Delta x_i}\right],$$

where x is any independent variable.
Time differencing (18) yields

$$\frac{D^{n+1}-D^{n-1}}{2\Delta t}=-\nabla^2 p+S^n, \tag{19}$$

where S^n is the second term on the right-hand side of (18). The usual procedure is to set $D^{n+1} = 0$ but to compute the small but non-zero divergence D^{n-1} due to machine round-off errors, and iterate (19) to obtain a pressure which compensates for it in equations (13) and (15).

The Poisson equation is solved by an ADI iterative approach as

$$\left(r_l-\frac{1}{r}\frac{\partial}{\partial r}r\frac{\partial}{\partial r}\right)p_{i,k}^l=\left(r_l+\frac{\partial^2}{\partial z^2}\right)p_{i,k}^l-S_{i,k},$$

$$\left(r_l-\frac{\partial^2}{\partial z^2}\right)p_{i,k}^{l+1}=\left(r_l+\frac{1}{r}\frac{\partial}{\partial r}r\frac{\partial}{\partial r}\right)p_{i,k}^l-S_{i,k},$$

where r_l are the iteration parameters with l denoting the iteration numbers. $p_{i,k}$ is the pressure and $S_{i,k}$ the source term on the grid point (i, k). The continuum second derivative operators are understood to represent their appropriate finite-difference analogues. The boundary conditions on the pressure are of the Neuman type, $\partial p/\partial s = G$, where s is the distance normal to the boundary and G is obtained from (15) by applying it on the boundary. The optimum iteration parameters are calculated by the method outlined in Wachpress (1966). This method minimizes the maximum eignenvalue of the iteration matrix.

Restrictions on the time step are due to the finite differencing of the terms. The non-

linear terms are subject to the Courant–Friedrichs–Lewy condition of $\Delta t \leqslant \Delta s/u_0$, where Δs is the smallest grid spacing and u_0 is the largest velocity. The time centring of the Coriolis terms results in a time-step restriction of $\Delta t \leqslant 1/2\Omega$. For the viscous terms the condition $\Delta t/\Delta s < 1$ should be satisfied for the finite-difference equation to correspond to a continuum equation and for the round-off error to be small. The non-physical computational mode which arises from the finite differencing of the non-linear terms when a first-order equation in time is rasied to a second-order difference equation is eliminated by periodic averaging of the variables.

4. Experimental results

4.1. *Homogeneous secular spin-up*

A single laboratory experiment was conducted to study the slow secular spin-up of a homogeneous fluid.† Both water baths were held at the same temperature (near room temperature) to eliminate any initial density stratification. The values of the governing parameters during the experiment were: $\Omega_0 = 1{\cdot}02\ \mathrm{s}^{-1}$, $d\Omega/dt = 5{\cdot}71 \times 10^{-4}\,\mathrm{s}^{-2}$, $R = 2{\cdot}48 \times 10^{-2}$, and $E = 4{\cdot}96 \times 10^{-4}$. The basic rotation period was $2\pi/\Omega_0 = 6{\cdot}2$ s and the homogeneous spin-up time scale was $T_s = 44{\cdot}0$ s, or only 7·1 rotational periods. The azimuthal velocity was measured using two neutrally buoyant floats of small size (diameter less than 0·05 cm). The horizontal positions of the plastic beads were periodically recorded on film using a slowly strobed horizontal beam of collimated light. The centre of the 0·7 cm thick light beam was located 0·3 cm above the mid-plane of the cylinder. The two floats were placed radially between

$$0{\cdot}5r_0 < r < 0{\cdot}65r_0,$$

and thus were located in the interior of the fluid.

In the limit of vanishing stratification, the Ekman suction is felt throughout the fluid, and the theoretical interior horizontal velocity components, given by

$$\left.\begin{aligned} u_2 &= -\tfrac{1}{2}r(1-e^{-t}),\\ v_0 &= r(t+e^{-t}-1),\end{aligned}\right\} \tag{20}$$

become depth-independent (a consequence of the Taylor–Proudman effect). Since the two beads were at different mean radii, we have plotted in figure 5 the observed and theoretical (20) azimuthal velocities in terms of the non-dimensional angular velocity v_0/r. Despite the relatively large estimate of the experimental errors, the observed data shows good agreement with theory for homogeneous secular spin-up. As the container starts to accelerate in the azimuthal direction, the interior of the fluid initially continues to rotate at its original angular velocity due to conservation of angular momentum. (In the accelerating reference frame, $v_0(AF) = r(e^{-t}-1)$.) With increasing time, the velocity difference between the container and fluid interior increases until the Ekman suction becomes sufficiently large for a balance to occur between the angular acceleration of the container and interior vortex stretching. The

† Weidman (1976) has examined the rapid secular spin-up and spin-down of a homogeneous fluid and found that non-linear effects become important when $T_A \lesssim T_S$, where T_A is the characteristic acceleration time scale defined by ${}_AT = \Omega_0/|d\Omega/dt|$. The one experiment discussed here was conducted within the linear regime since $T_A/T_S = 1/R \gg 1$.

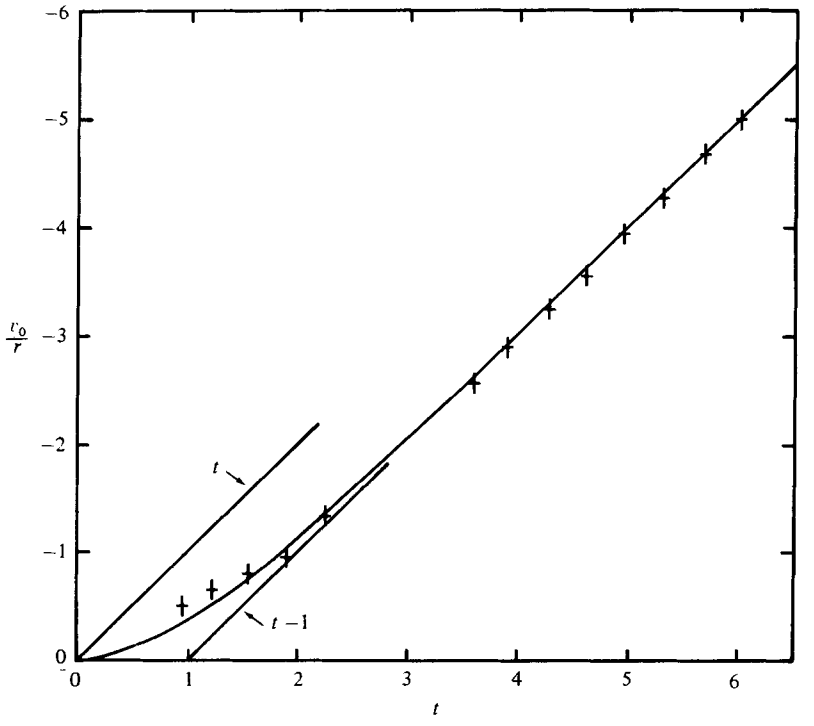

FIGURE 5. Comparison of observed and theoretical (20) angular velocities in fluid interior during secular homogeneous spin-up. The angular velocity of the container follows the line t while the interior fluid after spin-up follows the asymptote $t-1$.

Ekman flux is returned to the interior uniformly in z via the $E^{\frac{1}{2}}$ side-wall layer so that both the total vorticity ($\langle\zeta_0\rangle = 2\pi r v_0$) and the net angular momentum of the interior fluid increase with time. After several spin-up periods have elapsed, the angular velocity of the interior fluid lags the container by a constant amount (equal to $(d\Omega/dt)T_s$ in dimensional units).

A single numerical experiment was conducted to both test the code and simulate the homogeneous laboratory experiment. The numerical results both confirm the homogeneous secular spin-up process described here and indicate that the inertial modes of the basin are only weakly excited by the secular forcing. The difference between the scaled numerical azimuthal velocity at the interior point ($r = 0{\cdot}5r_0$, $z = 0$) and (20) is plotted in figure 6; the lowest inertial mode (with a period $T_i = 4{\cdot}3$ s) is just barely discernible in sharp contrast with the instantaneous spin-up results presented by Warn-Varnas *et al.* (1978). Since integration in time of the instantaneous forcing and response yields the secular forcing and response, the inertial modes in the secular case are reduced by a factor $T_i/4\pi T_s$, which is quite small (about 0·008) for the lowest axisymmetric inertial mode in this experiment. Figure 6 also indicates that the fluid spin-up occurs slightly faster in the numerical simulation than predicted by the analytic solution (20); the difference is small, however, and the negative trend shown in figure 6 could be removed if the dimensional spin-up time scale used to compute the theoretical solution was reduced by 1·2%.

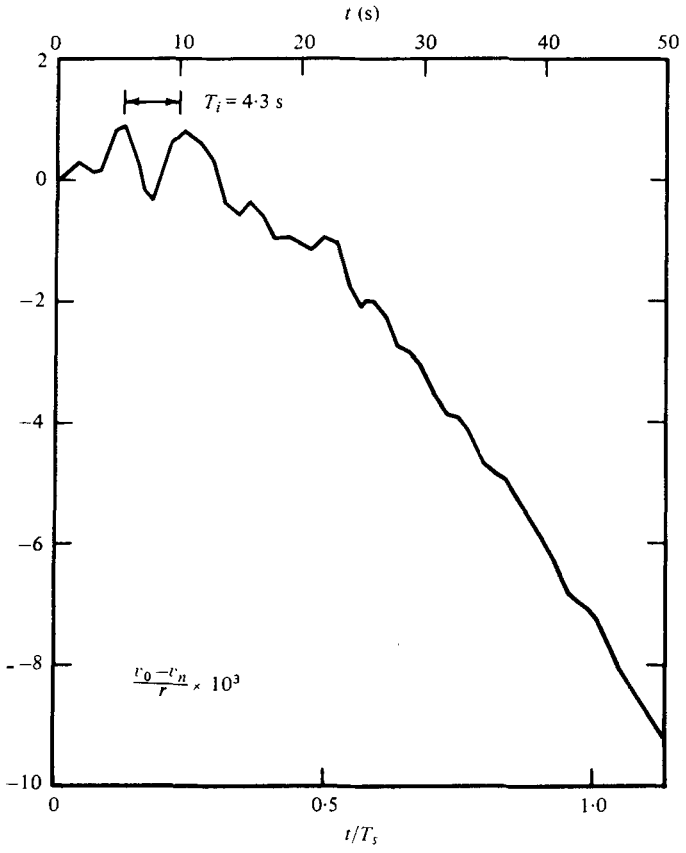

FIGURE 6. Difference in angular velocity at mid-depth and mid-radius between theoretical model (20) and numerical experiment. T_i is the period of the lowest inviscid natural inertial mode of the cylindrical container.

4.2. *Stratified secular spin-up*

Several laboratory experiments were conducted to study secular spin-up in a thermally stratified rotating fluid. The dimensions of the cylindrical container and the assumed constant thermodynamic properties of the silicone oil used as the working fluid are given in table 1. The values of the various experimental parameters for the individual experiments are listed in table 2. Essentially, two sets of experiments were conducted corresponding to values of the Burger number of $B = 0{\cdot}64$ and $1{\cdot}25$. The basic rotation rate Ω_0 was varied to change B since the overall temperature contrast between the upper and lower water baths was held approximately constant. Several experiments were conducted with different angular acceleration rates to study the effect of increasing Rossby number on the same basic initial state. We found that, for both values of B, the scaled temperature data from the different experiments agreed within experimental uncertainty, indicating that the observed temperature field behaved in a linear manner over the parameter range† $0{\cdot}16 \lesssim R/E^{\frac{1}{2}} \lesssim 1{\cdot}5$. For this reason we will describe the results of just one laboratory experiment [labelled no. 37

† A linear dependence on R was also found by Saunders & Beardsley (1975) in the instantaneous stratified spin-up experiments over the parameter range $1{\cdot}1 \lesssim R/E^{\frac{1}{2}} \lesssim 11{\cdot}0$.

$H = 4{\cdot}445$ cm, $R = 10{\cdot}03$ cm, $\nu = 0{\cdot}01172$ cm^2/s,
$\alpha = 0{\cdot}00134$/°C, $\kappa = 0{\cdot}000837$ cm^2/s, $\sigma = 14{\cdot}0$, $\rho_0 = 0{\cdot}818$ g/cm^3.

TABLE 1. Values of fixed or assumed constant experimental parameters.

Experiment no.	Ω_0 (rad/s)	T_s (s)	$T_s\Omega_0/2\pi$	$10^{+2}R$	$10^{+2}E^{\frac{1}{2}}$	N^2 (rad^2/s^2)	B
35	1·076	39·6	6·8	0·37	2·35	1·876	0·637
36	1·075	39·6	6·8	1·73	2·35	1·891	0·639
N1	1·069	39·7	6·8	2·12	2·35	1·898	0·644
37	1·069	39·7	6·8	3·31	2·35	1·898	0·644
50	0·551	55·3	4·9	4·77	3·28	1·898	1·249
51	0·552	55·3	4·9	2·40	3·28	1·898	1·248
52	0·551	55·3	4·9	1·21	3·28	1·906	1·253
53	0·551	55·3	4·9	0·62	3·28	1·913	1·256

TABLE 2. Values of experimental parameters for laboratory and one numerical (N1) secular spin-up experiments discussed in text. See text for parameter definitions.

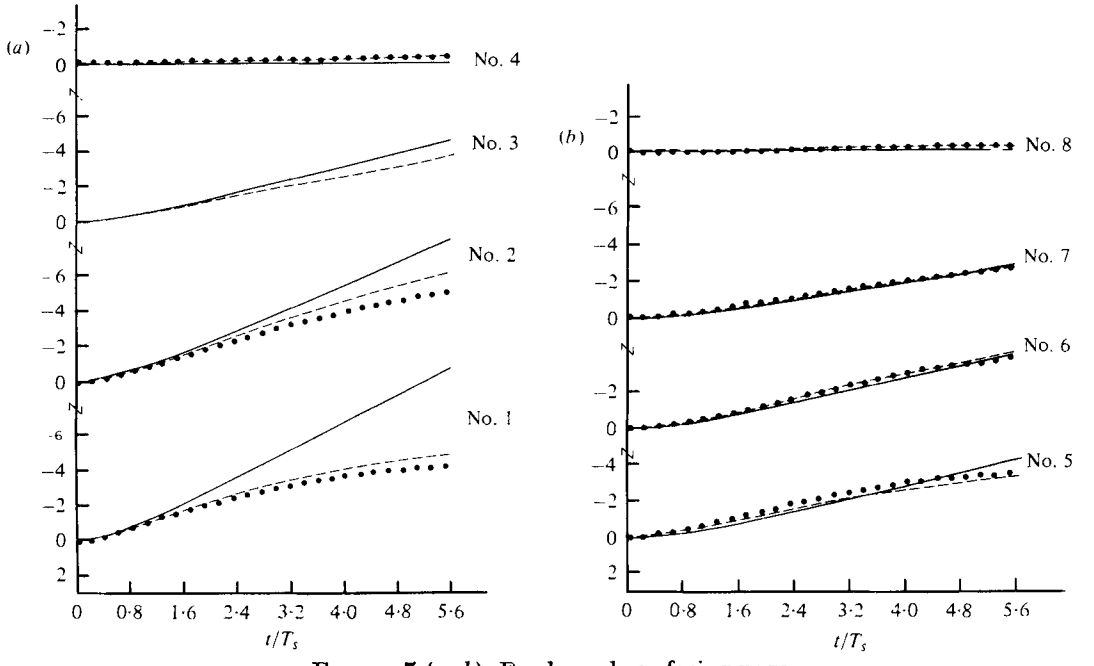

FIGURE 7 (*a*, *b*). For legend see facing page.

in table 2], and compare it with both the model presented in § 2 and the results of one numerical experiment (denoted N1 in table 2), conducted within this parameter range. The Rossby number R was the only external parameter which differed between the two experiments (no. 37 and N1). The estimated measurement error in the laboratory temperature data obtained in experiment no. 37 is $\pm 0{\cdot}0052$ °C or $\pm 4\%$ of the

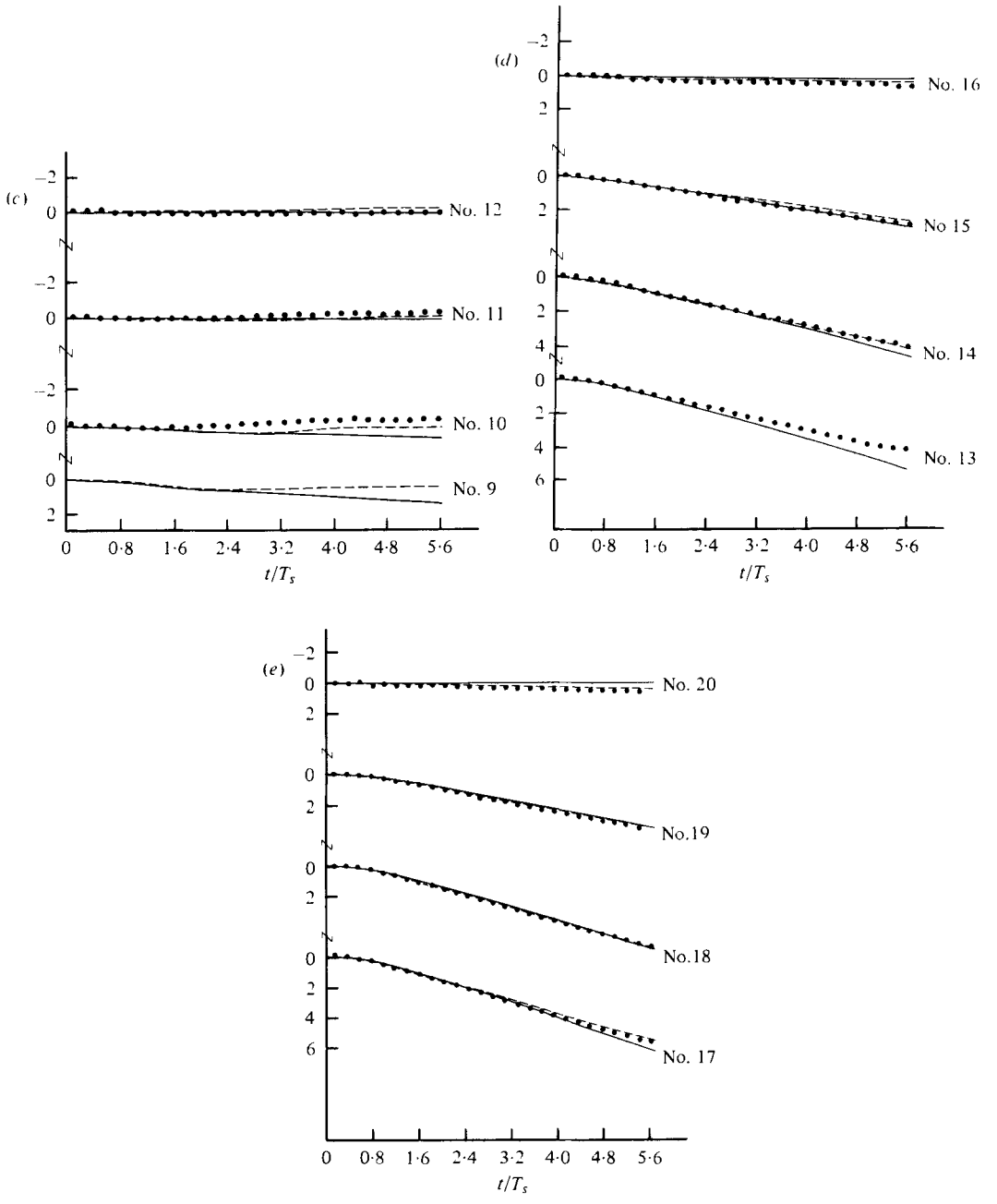

FIGURE 7. Comparison of non-dimensional perturbation temperatures: ..., laboratory experiment no. 37; ----, numerical experiment N1; ——, theoretical perturbation temperatures predicted by (12). Positive temperature deviations are plotted downward so that the data correspond to non-dimensional density, with positive density deviations plotted upward. Thermistor number shown to right of corresponding data. The radial locations of the different time series are (*a*) $r = 0{\cdot}9375r_0$, (*b*) $r = 0{\cdot}875r_0$, (*c*) $r = 0{\cdot}75r_0$, (*d*) $r = 0{\cdot}5r_0$, and (*e*) $r = 0$.

perturbation temperature scale, $\Omega_0 V/\alpha g$. The centrifugal component of the gravitational potential has been ignored in both theoretical and numerical models on the assumption that the steady-state Sweet–Eddington flow would be quite weak in the actual experiments. In fact, Barcilon & Pedlosky (1967) show in their theoretical study of Sweet–Eddington flow that the maximum azimuthal velocity V_{SE} scales like

$$V_{\mathrm{SE}} = (2\nu^{\frac{1}{2}}\Omega_0^{\frac{5}{2}} H r_0)/g\sigma$$

in the convection regime (see their equation 4.30). In the secular stratified spin-up experiments described here, V_{SE} was always $\leqslant 1\%$ of the spin-up velocity scale V given in (1), so that the neglect of centrifugal effects is indeed justified here.

We will now briefly describe the stratified secular spin-up process defined by the asymptotic model developed in § 2. We saw in the homogeneous secular spin-up case that the Taylor–Proudman effect constrains the interior horizontal flow to be independent of depth and that the important meridional secondary circulation is closed by passive viscous boundary layers on the side wall. In a container with perfectly insulating side walls, rather weak thermal stratification effectively inhibits vertical motion in the side-wall boundary layers, thus forcing the Ekman-layer flux to return directly to the interior via 'jets' in the corner regions of the container. In the asymptotic theory, the orientation of this jet is slowly varying over the spin-up time scale, so that the pattern of the meridional circulation does not change much with time, especially for t greater than about $1{\cdot}5T_s$. The resulting weak vertical advection of the (initially level) constant temperature surfaces creates the perturbation temperature field. Since the interior flow is to lowest order geostrophic and hydrostatic, the thermal wind relationship (3) holds with $V_{0z} = -\frac{1}{2}T_0 r$. As the radial temperature increases with time over the inner region of the lower interior, the vertical shear of v_0 becomes more negative, causing the layer of fluid adjacent to the lower Ekman layer to accelerate more rapidly. Conservation of potential vorticity over the spin-up time scale implies an inward radial shift of positive vorticity without changing the total vorticity within each horizontal layer, and thus the interior azimuthal velocity $v_0(r_0)$ at the side wall remains zero. Actually, the accelerating side wall acts as a source of positive vorticity which quickly diffuses into the fluid, creating the transient $E^{\frac{1}{4}}$ layer required to satisfy the no-slip condition on the side wall.

The non-dimensional perturbation temperatures observed in the laboratory (no. 37) and numerical (N1) experiments are compared in figure 7 with the theoretical solution (12) given in § 2. The data from each working thermistor is shown as solid circles in figure 7 and has been organized by the radial and vertical position of the thermistors. The reference number and position of each thermistor is shown in figure 3. The numerical and theoretical behaviour at each thermistor location is shown by dashed and solid lines, respectively. We have chosen to reverse the temperature axis so that negative temperature deviations which correspond to positive density deviations are plotted upward. In general, the observed and predicted perturbation temperature fields agree rather well. A continual upwelling of colder, denser fluid occurs near the outer edge of the basin with a broad downwelling of warmer, lighter fluid over most of the lower interior of the fluid to complete the meridional circulation. The quantitative agreement between experiments and theory is best near the centre of the basin. The major difference occurs near the side wall where the outermost ring of

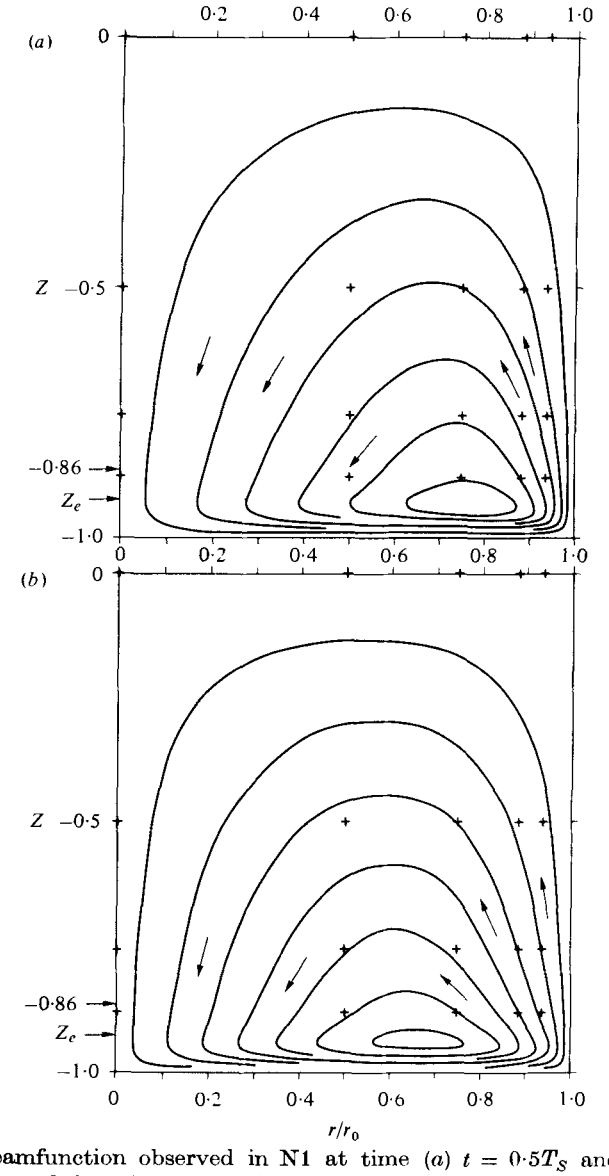

FIGURE 8. Streamfunction observed in N1 at time (*a*) $t = 0{\cdot}5T_S$ and (*b*) $t = 4{\cdot}0T_S$. Crosses indicate locations of thermistors used in laboratory experiment. The height of the theoretical radial velocity node in the lower Ekman layer is shown by Z_e, where $1 + Z_e = \pi E^{\frac{1}{2}}$.

thermistors quickly becomes enveloped by the growing $E^{\frac{1}{2}}$ layer. The experimental temperature data at thermistors no. 1 and no. 2 follow the theoretical prediction closely until $t \sim 1{\cdot}5T_s$, then exhibit a slower increase with time than the essentially linear rise predicted. Both the vertical and radial temperature gradients are smaller than predicted near the lower, outer corner. The experimental data observed at thermistors no. 9 and no. 10 (see figure 7*c*) show a slight reversal in the secular temperature behaviour which indicates that the actual circle of downwelling is smaller than predicted.

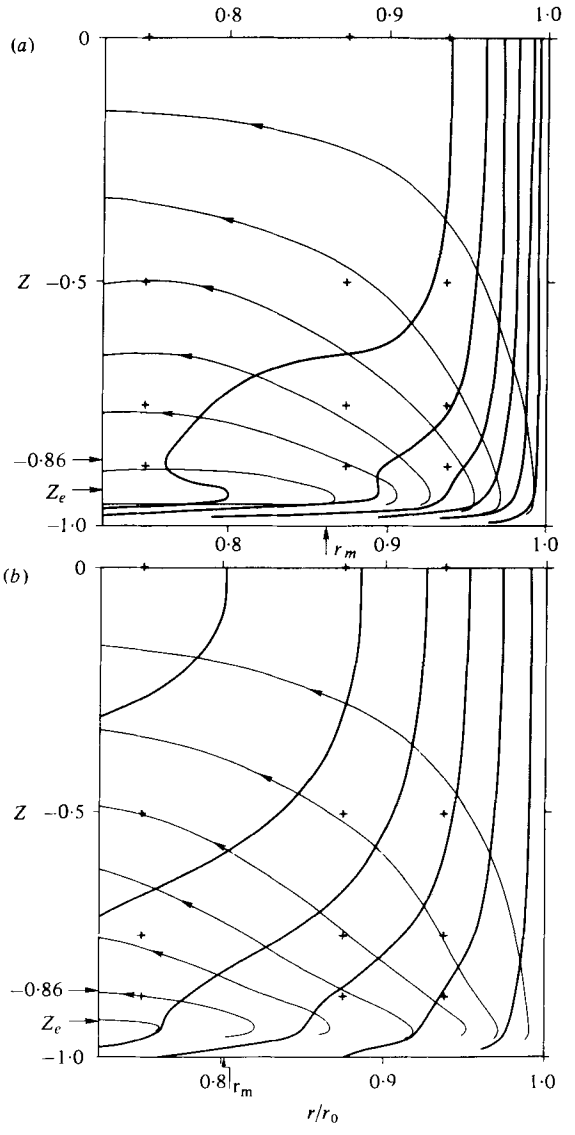

FIGURE 9. Enlarged contour plots of the streamfunction and azimuthal velocity v_0 observed in N1 at time (*a*) $t = 0{\cdot}5T_S$ and (*b*) $t = 1{\cdot}0T_S$. Crosses indicate thermistor locations. The height of the radial velocity node is shown by Z_e, where $(1 + Z_e) = \pi E^{\frac{1}{2}}$. The radial location of the maximum streamfunction predicted at $Z = -1$ by (10) is indicated by r_m.

The numerical model streamfunction is shown at time $t = 0{\cdot}5T_s$ and $4{\cdot}0T_s$ in figure 8. For reference, the (theoretical) height of the radial velocity node in the lower Ekman layer is indicated by Z_e, where $(1 + Z_e) = \pi E^{\frac{1}{2}}$. The thermistor locations are indicated by small crosses. The orientation of the lower corner jet does not change much over time, although the location of the maximum of the streamfunction does move slowly towards the centre with time. While the interior downwelling and vortex stretching is more intense near the lower Ekman layer, the non-dimensional vertical penetration scale for the lowest theoretical mode is large enough ($\delta_v \sim r_0/\alpha_n B = 0{\cdot}92$) that the

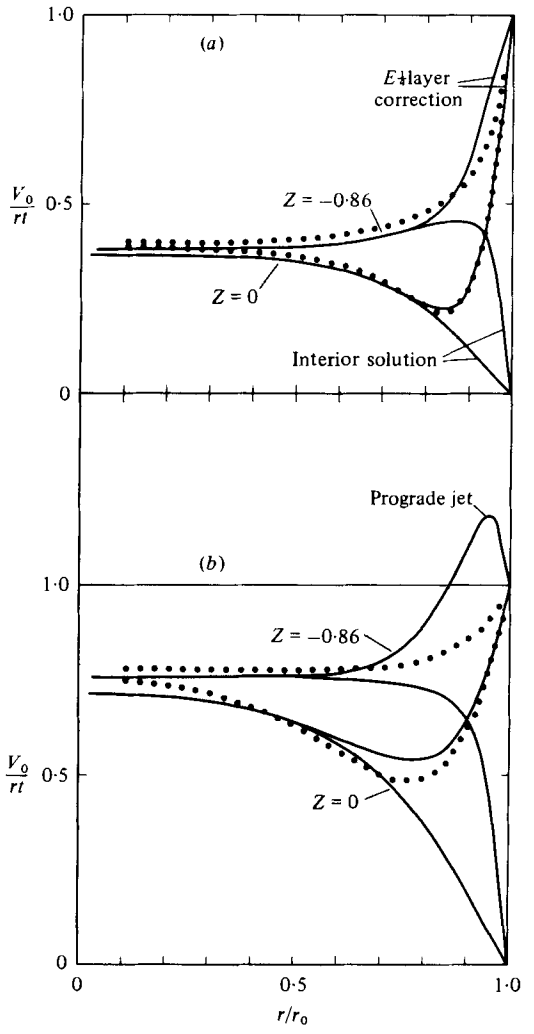

FIGURE 10. Comparison of non-dimensional angular velocity divided by time at time (*a*) $t = 1{\cdot}0T_S$ and (*b*) $t = 4{\cdot}0T_S$: ····, observed in N1; ——, predicted by (11). The interior solution is shown with and without the $E^{\frac{1}{4}}$ layer correction. The profiles are shown at two levels, the mid-plane at $Z = 0$, and at $Z = -0{\cdot}86$, just above the lower Ekman layer.

secondary circulation occurs throughout the interior of the basin. Thermistors 1–8 and 13–20 are clearly located in the upwelling and downwelling zones respectively. As shown in figure 7*c*, weak upwelling occurs with increasing time at thermistors 9–12 located at $r = 0{\cdot}75$. This effect is better illustrated in figure 9, where the numerical streamfunction is shown for $r \geqslant 0{\cdot}72$. The radial position of the maximum of the interior streamfunction predicted at $z = -1$ by (10) is indicated in figure 9 by r_m. Since $w = r^{-1}\Psi_r$, upwelling out of the lower Ekman layer occurs over a wider ring in the laboratory and numerical experiments than predicted by theory.

The interior azimuthal velocity spin-up near the lower boundary is illustrated in figure 9, where we have plotted contours of v_0 scaled by the side-wall value. The pronounced inward advection of the v_0 contours near the lower corner is caused by the

Coriolis acceleration on radial displacement, i.e. $v_{0t} = -2u_2$. The v_0 contours closely parallel the side wall, especially near the midplane of the basin at $z = 0$ during the early phases of spin-up. This structure illustrates the initial one-dimensional character of the transient $E^{\frac{1}{4}}$ layer.

A comparison between the theoretical (11) and numerical non-dimensional angular velocity scaled by time is shown in figure 10. The comparisons are made for two levels: the mid-plane ($z = 0$) and just above the lowest thermistors at $z = -0{\cdot}86$ (see figures 8 or 9). Figure 10 indicates that the simple one-dimensional $E^{\frac{1}{4}}$ boundary-layer correction agrees well with the numerical v_0 profile at $z = 0$ throughout spin-up. At the lower level ($z = -0{\cdot}86$) which intersects the corner 'jet', the theoretical boundary-layer correction term overestimates the azimuthal velocity near the side wall. This effect, noticeable at $t = 1{\cdot}0T_s$, becomes pronounced by $t = 4{\cdot}0T_s$, when the theory predicts the formation of a prograde zonal jet with azimuthal velocities greater than the maximum velocity occurring at the side wall. As a ring of fluid enters the interior from the corner region, its radius about the rotation axis contracts and the azimuthal velocity increases by angular-momentum conservation. The viscous diffusion of positive vorticity from the accelerating side wall produces an additional positive torque on the fluid ring so that a net prograde velocity can occur on contraction. Since *no* prograde motion was observed in the numerical experiment, we conclude that the simple superposition of the interior and one-dimensional transient $E^{\frac{1}{4}}$ layer solutions contained in (11) breaks down near the corner region where a more complete theory is clearly needed. If a fluid ring near the corner entered the interior from a maximum radius which is less than predicted, the resulting azimuthal velocity would be less. Thus, the observed lack of a prograde jet is consistent with the experimentally observed inward increase in the radial width of the upwelling zone. Near the centre of the basin, angular velocity observed in N1 is slightly faster than predicted. Near $r = 0$, the observed and predicted velocities agree if the theoretical spin-up time scale T_s is decreased by 5–8 %.

5. Conclusion

We have examined the secular spin-up of a thermally stratified fluid in both a laboratory and a numerical model and find good qualitative agreement between the observed interior temperature and azimuthal velocity fields and the simple asymptotic theory presented in § 2. The structure of the transient side-wall boundary layer becomes more complicated near the corner regions where we believe the additional vorticity added through lateral viscous diffusion causes a decrease in the vertical flux out of the lower Ekman layer near the corner. This in turn forces an inward shift of the upwelling zone since the net outflux from the bottom Ekman layer is controlled through continuity by the difference between the interior and bottom boundary vorticity and should remain relatively constant in time after $t \sim 1{\cdot}5T_s$. The streamfunction maximum observed in N1 varied less than 5 % over the time interval between 1·5 and $5{\cdot}0T_s$.

The relatively good agreement between experiment and theory found in these secular spin-up experiments is in sharp contrast with the results of the instantaneous spin-up experiments summarized in § 1. The experimental spin-up time scale was about 5–8 % faster than predicted in the secular case while, in the instantaneous case,

the lowest mode spin-up time was roughly 30–60 % faster than predicted. The difference is due to the very weak excitation of inertial–gravity-wave transients in both homogeneous and stratified numerical experiments by the secular forcing. Thus the asymptotic theory which has filtered out these initial higher-frequency transients is accurate even though the inertial period is not much smaller than the spin-up time scale.

The authors would like to thank Drs L. Howard at M.I.T. and S. Piacsek at NORDA for their interest and helpful comments made during the course of this research. The laboratory experiments were conducted in 1972 in the Geophysical Fluid Dynamics Laboratory, Department of Meteorology, M.I.T. with the support of NSF grant A-30616X1. The numerical work was performed at and supported by NORDA. The interpretation of the experimental work and preparation of this manuscript has been supported by NSF through grants OCE73-00528 and OCE76-01813.

REFERENCES

ALLEN, J. C. 1973 Upwelling and coastal jets in a continuously stratified ocean. *J. Phys. Oceanog.* **3**, 245–257.

BARCILON, A., LAU, J., PIACSEK, S. & WARN-VARNAS, A. 1975 Numerical experiments on stratified spin-up. *J. Geophys. Fluid Dyn.* **7** (1), 29–42.

BARCILON, V. 1968 Stewartson layers in transient rotating fluid flows. *J. Fluid Mech.* **33**, 815–825.

BARCILON, V. & PEDLOSKY, J. 1967 On the steady motions produced by a stable stratification in a rapidly rotating fluid. *J. Fluid Mech.* **29**, 673–690.

BENTON, E. R. & CLARKE, A. R. 1974 Spin-up. *Ann. Rev. Fluid Mech.* **6**, 257–280.

BLUMSACK, S. L. 1972 The transverse circulation near a coast. *J. Phys. Oceanog.* **2**, 34–40.

BUZYNA, G. & VERONIS, G. 1971 Spin-up of a stratified fluid: theory and experiment. *J. Fluid Mech.* **50**, 579–608.

CLARK, A., CLARK, P. A., THOMAS, J. H. & LEE, N. H. 1972 Spin-up of a strongly stratified fluid in a sphere. *J. Fluid Mech.* **45**, 131–149.

GREENSPAN, H. P. 1968 *The Theory of Rotating Fluids.* Cambridge University Press.

GREENSPAN, H. P. & HOWARD, L. N. 1963 On a time dependent motion of a rotating fluid. *J. Fluid Mech.* **17**, 385–404.

HOLTON, J. R. 1965 The influence of viscous boundary layers on transient motions in a stratified rotating fluid. Parts 1 and 2. *J. Atmos. Sci.* **22**, 402–411, 535–540.

PEDLOSKY, J. 1968 An overlooked aspect of the wind-driven oceanic circulation. *J. Fluid Mech.* **32**, 809–821.

PIACSEK, S. A. & WILLIAMS, G. P. 1970 Conservation properties of convection difference schemes. *J. Comp. Phys.* **6**, 392.

SAKURAI, T. 1969 Spin-down problem of rotating stratified fluid in thermally insulated circular cylinders. *J. Fluid Mech.* **37**, 689–699.

SAKURAI, T., CLARK, A. & CLARK, P. 1971 Spin-down of a Boussinesq fluid of small Prandtl number in a circular cylinder. *J. Fluid Mech.* **49**, 753–773.

SAUNDERS, K. D. & BEARDSLEY, R. C. 1975 An experimental study of the spin-up of a thermally stratified rotating fluid. *J. Geophys. Fluid Dyn.* **7** (1), 1–28.

SIEGMANN, W. L. 1967 Spin-up of a continuously stratified fluid. M.S. thesis, Department of Mathematics, M.I.T., Cambridge, Mass. 02139.

ST-MAURICE, J-P. & VERONIS, G. 1975 A multi-scaling analysis of the spin-up problem. *J. Fluid Mech.* **68**, 417–445.

WACHPRESS, E. L. 1966 *Iterative Solution of Elliptic Systems.* New York: Prentice-Hall.

WALIN, G. 1969 Some aspects of time-dependent motion of a stratified rotating fluid. *J. Fluid Mech.* **36**, 289–307.

WARN-VARNAS, A., FOWLIS, W. W., PIACSEK, S. & LEE, S. M. 1978 Numerical solutions and laser Doppler measurements of spin-up. *J. Fluid Mech.* **85**, 609–639.

WEIDMAN, P. D. 1976 On the spin-up and spin-down of a rotating fluid. Part 1. Extending the Wedemeyer model. Part 2. Measurements and stability. *J. Fluid Mech.* **77**, 685–735.